Resonant thermocapillary and buoyant flows with finite frequency gravity modulation

V. A. Suresh, C. I. Christov,[a] and G. M. Homsy[b]
Department of Chemical Engineering, Stanford University, California 94305-5025

(Received 22 February 1999; accepted 27 May 1999)

Interaction between a base thermocapillary flow and a time-dependent buoyant force is studied for a slot geometry. A temperature gradient applied along a fluid-filled slot with thermocapillarity at a free surface produces a base parallel flow. The system is subjected to streamwise gravitational acceleration that varies harmonically in time. Grassia and Homsy [Phys. Fluids. **10**, 1273 (1998)] have shown that in the limit of zero frequency modulation, coupling of the thermocapillary flow with long wave convective modes leads to singularities at critical points corresponding to the Rayleigh–Bénard eigenvalues. In the case of small but finite frequency modulation studied here, inertial effects moderate the singularities which are replaced by a response that scales exponentially with the inverse of the dimensionless modulation frequency. An $O(1)$ delay is observed in the onset of the resonant response even for small modulation frequencies. The response is also found to scale exponentially with the inverse Prandtl number for large Prandtl numbers and to be independent of Prandtl number for small Prandtl numbers. Relaxation oscillations are observed in certain parameter ranges as a result of the coupling between the fluid and thermal fields. A Galerkin approximation is used to reduce the problem to an equivalent dynamical system, the analysis of which gives analytical support to and insight into the numerical results. © *1999 American Institute of Physics.* [S1070-6631(99)03809-X]

I. INTRODUCTION

One of the widely studied problems concerning body-force-driven flows has been that of a fluid in a nonuniform temperature field acted upon by gravity. Theoretical treatments have dealt with the classical Rayleigh–Bénard problem of a fluid layer heated from below in a vertical gravitational field (see, e.g., Ref. 1) as well as the coupling of vertical gravity and an applied horizontal temperature difference.[2] There have also been studies on the effect of time modulated gravity on instabilities[3] and on flows driven by horizontal gradients.[4] Recent studies of the effect of time-dependent gravity or ''jitter'' (e.g., Ref. 5) have been motivated by the need to model fluid processes under microgravity conditions on board spacecraft. Under these conditions, arbitrarily oriented gravitational fluctuations give rise to body forces and affect flows that would otherwise be steady. It has been shown that such time-dependent forces can significantly affect the stability of the system[3] and therefore there is a growing interest in understanding these flows.

Many such studies have focused on the effect of jitter on convective states driven by mean gravity.[4,6] However, it is also possible to consider the interaction of jitter with convective states resulting from a driving force different from buoyancy. Grassia and Homsy have studied such flows in which jitter interacts with a base thermocapillary flow.[7] Such interactions are an important factor in understanding material processing flows in microgravity conditions, since these flows commonly involve interfacial tension gradients that drive Marangoni flows. Grassia and Homsy used a time harmonic acceleration to model the fluctuating body force. They restricted attention to a slot geometry in order to reduce mathematical complexity. In this study, we use the same physical model for our system. The system, shown in Fig. 1, consists of a two-dimensional fluid-filled slot of infinite extent in the x direction and thickness d in the y direction. The lower boundary is rigid and insulating while the upper boundary has an insulating free interface. A constant temperature gradient β is applied along the length of the slot and the usual Boussinesq approximation is made. The temperature gradient sets up a thermocapillary flow in the slot with a velocity scale $U_{tc}=d\gamma_T\beta/\mu$, where γ_T characterizes the variation of surface tension with temperature and μ is the mean viscosity of the fluid. Following Ref. 7, we assume the base flow to be a local return flow, so that the streamlines are parallel. We also assume that the capillary number $\mu U_{tc}/\sigma_0$, where σ_0 is the mean surface tension of the fluid, is sufficiently small for the free interface at the top to remain flat. The flow distorts the isotherms and leads to temperature gradients in both the x and y directions. A time harmonic gravitational acceleration of amplitude g and frequency ω is imposed in the plane of the flow. It can be considered as an approximation of the jitter, consisting of a single term from the Fourier decomposition of the time-dependent fluctuations. The interaction between the modulated gravity and the applied and/or convected temperature gradients leads to a buoyant force acting on the fluid. The system alternates between stable and unstable configurations as the buoyant flow

[a]Present address: Department of Mathematics, University of Southwestern Louisiana, Lafayette, LA 70504-1010.
[b]Corresponding author. Electronic mail: bud@chemeng.stanford.edu

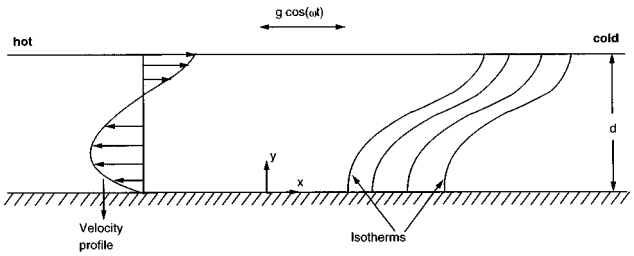

FIG. 1. Definition sketch. An imposed lateral temperature gradient establishes a thermocapillary return flow as shown, which is then subjected to horizontal jitter.

alternately opposes and enhances the base flow. We have adopted the sign convention in Ref. 7, i.e., buoyancy enhances the base flow when $\cos(\omega t)$ is positive.

The modulation imposes a time scale on the system given by its time period of oscillation, $2\pi/\omega$. It is convenient to use this time scale to define a dimensionless time $t = \omega \bar{t}$. Molecular processes in the fluid give rise to two other time scales, the viscous diffusion time d^2/ν, where ν, is the kinematic viscosity, and the thermal diffusion time d^2/κ, where κ is the mean thermal diffusivity of the fluid. The Stokes number, $\Omega = \omega d^2/\nu$, defines a dimensionless modulation frequency as the ratio of the viscous equilibration time to the time scale of the modulation and is a measure of the fluid inertia. Similarly $\mathrm{Pr}\Omega = \omega d^2/\kappa$, where $\mathrm{Pr} = \nu/\kappa$ is the Prandtl number, is a measure of the thermal inertia of the fluid.

Lengths are scaled with the slot height d and velocities with the thermocapillary velocity U_{tc}. The temperature scale is $d\mathrm{Ma}\beta$, where $\mathrm{Ma} = U_{tc} d/\kappa$ is the Marangoni number. The other relevant dimensionless group is the Rayleigh number $\mathrm{Ra} = g d^4 \alpha_T \beta/\nu\kappa$, where α_T is the coefficient of thermal expansion of the fluid with $\mathrm{Ra}\cos(t)$ being a measure of the instantaneous buoyant force.

In this work we investigate the effect of coupled thermocapillarity and buoyancy on parallel flows. It was shown in Ref. 7 that the coupled flow remains parallel only when gravity is confined to the plane of flow. Further, it is clear that the vertical thermal stratification produced by the base flow is stable with respect to constant vertical gravity, but can become unstable in the presence of vertical modulation: the resulting convective cells are finite wavelength modes that are not associated with parallel flows, but will be analogous to those studied in Ref. 3. Our focus is on long-wave modes which occur for horizontal modulation. In this case, the thermocapillary flow breaks the symmetry of the modulated Rayleigh–Bénard convection by imposing flow in a particular direction. Streamwise gravity interacts with the convected vertical temperature gradients to produce vorticity. In the part of the cycle when the applied stratification is unstable, the vorticity produced enhances the vertical gradients which themselves can couple with the streamwise gravity. Thus there is a complicated interaction between the modulated gravity and the temperature gradients leading to a rich class of behaviors even with the restriction to parallel flows.

Streamwise modulation was studied in the quasistatic limit of zero frequency modulation in Ref. 7 and analytic solutions for the stream function, velocity, and temperature were obtained for arbitrary magnitudes of the modulation. The fluid velocity and temperature were found to increase with $\mathrm{Ra}\cos(t)$ in the subcritical part of the cycle below the first Rayleigh–Bénard eigenvalue. However, these solutions broke down at the Rayleigh–Bénard eigenvalues since resonant interactions with long-wave convective modes led to unbounded fluid velocities and temperatures. The quasistatic analysis also predicted that the flow changes direction at the first Rayleigh–Bénard eigenvalue, causing the fluid to move in a direction opposite to the driving thermocapillary and buoyant forces during the supercritical part of the cycle when $\mathrm{Ra}\cos(t)$ increases beyond the eigenvalue. We seek to avoid these nonphysical results by studying the system behavior for small but finite frequencies in order to resolve the singularities and predict the flow in the supercritical regime.

The system under consideration has parallels to problems studied in dynamic bifurcation theory, which deals with changes in the qualitative behavior of a dynamic system as the bifurcation parameter is varied (see, for e.g., Ref. 8). The bifurcation parameter is commonly assumed to be independent of time. However, in many naturally occurring problems, it may vary slowly in time and it is of particular interest to determine the system behavior in this situation. Problems that involve slow passage through a bifurcation point exhibit two salient features.[9] First, ''jump transitions'' are observed in which there is a sudden and rapid change in the solution as the bifurcation parameter crosses the bifurcation point. Second, it is seen that the jump transition does not occur at the bifurcation point, but is delayed. This delay is often an $O(1)$ quantity even though the rate of change of the bifurcation parameter is very small.

In the present case, the system passes through a bifurcation point as the parameter $\mathrm{Ra}\cos(t)$ varies across the Rayleigh–Bénard eigenvalue. However, there are important differences between the situation in this problem and the standard problem of passage through a bifurcation point. In contrast with the commonly studied nonlinear problems of dynamic bifurcations, the system here remains linear even for the instability since we only consider long wave instability modes. Moreover, the bifurcation parameter $\mathrm{Ra}\cos(t)$ swings back and forth across the stability boundary determined by the Rayleigh–Bénard eigenvalue. Therefore, the solution alternates between the subcritical branch below the bifurcation point and the supercritical branch above the bifurcation point. We shall show that the amplitude of the response at the jump transition is determined by the finite response at the bifurcation point and the time spent in the supercritical part of the cycle.

The paper is organized as follows. In Sec. II we detail the governing equations and boundary conditions for the horizontally stratified slot with streamwise modulation. Next we present solutions of these equations. The special case of thermocapillary flow with no body forces is considered in Sec. III A. In Sec. III C the structure of the long-wavelength Rayleigh–Bénard modes is discussed and in Sec. III D numerical solutions of the governing equations are presented. The frequency and parametric dependence of the solutions

are examined. We find that inertial effects correct the unphysical predictions of the quasistatic solution and resonant interactions with the Rayleigh–Bénard eigenvalues lead to a large response in the vicinity of the eigenvalues which scales exponentially with the reciprocal of the modulation frequency. Coupling of the thermal and inertial fields is found to lead to relaxation oscillations. In Sec. IV we present an approximate theoretical analysis to explain the numerical results. We conclude in Sec. V with a summary of the results.

II. GOVERNING EQUATIONS

The problem definition and scalings have already been given in Fig. 1 and Sec. I, respectively. The system can be conveniently described using the vorticity equation written in terms of a streamfunction ψ defined such that $u=\psi_y$. Using the scalings described above, the dimensionless vorticity and energy equations can be written as

$$\Omega\psi_{yyt}=\psi_{yyyy}+\mathrm{Ra}\cos(t)T_y, \tag{1}$$

$$\Omega\mathrm{Pr}T_t=\psi_y+T_{yy}. \tag{2}$$

The vorticity equation represents a balance between fluid inertia, viscosity, and buoyancy. The heat equation balances thermal inertia with convection and molecular diffusion of heat. Thus the modulation frequency Ω is a measure of fluid inertia while the product $\mathrm{Pr}\Omega$ is a measure of thermal inertia.

Since the flow is a parallel flow intended to model a slot with distant end walls, continuity requires that the net flux of fluid at any cross section of the slot be zero. This local return flow condition enables us to specify ψ on the lower and upper boundaries:

$$\psi=0 \quad \text{at } y=0,1. \tag{3}$$

Using the no-slip condition at the bottom and the thermocapillary boundary condition on shear stress at the interface we obtain two more boundary conditions:

$$\psi_y=0 \quad \text{at } y=0, \quad \psi_{yy}=1 \quad \text{at } y=1. \tag{4}$$

Insulating boundary conditions require that

$$T_y=0 \quad \text{at } y=0,1. \tag{5}$$

III. RESULTS

A. Base thermocapillary return flow

In the absence of gravity a base parallel flow driven by thermocapillarity is present in the slot. In this case the governing equations (1) and (2) at steady-state simplify significantly:

$$\psi_{yyyy}=0, \tag{6}$$

$$\psi_y+T_{yy}=0. \tag{7}$$

This problem was studied by Sen and Davis[10] who found the solutions

$$\psi_{\mathrm{SD}}=\tfrac{1}{4}(y^3-y^2), \tag{8}$$

$$T_{\mathrm{SD}}=-x-\tfrac{1}{48}(3y^4-4y^3+1). \tag{9}$$

This solution is sketched in Fig. 1 and is often referred to as the ''thermocapillary return flow.'' The thermocapillary flow sets up temperature gradients in the y direction which interact with the imposed acceleration resulting in a buoyant force acting on the fluid. The coupling of buoyancy and thermocapillarity modifies the base flow and is the subject of this study.

B. Quasistatic approximation with modulation

The quasistatic approximation treated in Ref. 7 is obtained in the low-frequency limit by setting Ω identically equal to zero. In this case the equations can be decoupled and admit analytical solutions[7] which exhibit singularities at critical values of $\mathrm{Ra}\cos(t)$, $\cos(t)>0$. We do not repeat those details here. These values of $\mathrm{Ra}\cos(t)$ are identical to the Rayleigh–Bénard eigenvalues and so it is necessary to study the role played by the unstable Rayleigh–Bénard convective modes in this problem.

C. Rayleigh–Bénard modes

In the slot problem with applied horizontal stratification and constant horizontal gravity, unstable Rayleigh–Bénard modes are set up when the acceleration acts along the negative x direction. In this configuration the body force, which acts to displace the hot light fluid by the cold heavy fluid, enhances the return flow. Thus the symmetry of the Rayleigh–Bénard modes is broken by the thermocapillary flow. Since the singularities result from a resonant interaction between the base thermocapillary flow and the unstable convective modes, it is instructive to discuss the pure convective modes with constant gravity and no thermocapillarity for the slot problem.

Here we consider only parallel flow or long wave modes having infinite wavelength in the x direction.The governing equations for these modes are[1]

$$\psi_{yyt}=\psi_{yyyy}+\mathrm{Ra}T_y, \tag{10}$$

$$\mathrm{Pr}T_t=\psi_y+T_{yy}. \tag{11}$$

The homogeneous boundary conditions are

$$\psi=0, \quad \psi_y=0, \quad T_y=0 \quad \text{at } y=0, \tag{12}$$

$$\psi=0, \quad \psi_{yy}=0, \quad T_y=0 \quad \text{at } y=1. \tag{13}$$

At the onset of instability these modes pass through a stationary state where the time derivatives vanish and the equations can be decoupled to obtain

$$\psi_{yyyy}=\mathrm{Ra}\psi, \tag{14}$$

$$T=-\int_0^y \psi(s)\,ds. \tag{15}$$

Equation (14) with associated boundary conditions constitutes a eigenvalue problem with nonzero solutions only for certain values of the parameter $\chi_+^4=\mathrm{Ra}$. These solutions can be written as

$$\psi=H_1(y)\sinh(\chi_+)-J_1(y)\sin(\chi_+), \tag{16}$$

with

$$H_1(y)=\frac{\cosh(\chi_+ y)}{\cosh(\chi_+)}-\frac{\sinh(\chi_+ y)}{\sinh(\chi_+)}, \tag{17}$$

$$J_1(y)=\frac{\cos(\chi_+ y)}{\cos(\chi_+)}-\frac{\sin(\chi_+ y)}{\sin(\chi_+)}, \tag{18}$$

and χ_+ satisfies the eigenvalue relation

$$\tan(\chi_+)=\tanh(\chi_+). \tag{19}$$

All eigenvalues are well approximated by the formula $\chi_+ \approx (n+\frac{1}{4})\pi$ and the first eigenvalue occurs at $\chi_+ \approx 3.9265$, i.e., Ra$\approx$237.7.

Similarly, the eigenfunctions for temperature are given by

$$T=H_2(y)\sinh(\chi_+)-J_2(y)\sin(\chi_+), \tag{20}$$

with

$$H_2(y)=\frac{1}{\chi_+}\left(\frac{\cosh(\chi_+ y)}{\sinh(\chi_+)}-\frac{\sinh(\chi_+ y)}{\cosh(\chi_+)}\right), \tag{21}$$

$$J_2(y)=-\frac{1}{\chi_+}\left(\frac{\cos(\chi_+ y)}{\sin(\chi_+)}+\frac{\sin(\chi_+ y)}{\cos(\chi_+)}\right). \tag{22}$$

Equations (16) and (20) describe the structure of the Rayleigh–Bénard eigenmodes. We shall use these results to describe the resonant interactions of the thermocapillary flow and the Rayleigh–Bénard modes.

D. Effect of inertia

The quasistatic approximation corresponds to neglecting the fluid and thermal inertia of the system. Thus the resonant forcing of a noninertial system is responsible for the singularities observed in the quasistatic limit. In the finite frequency case we expect inertial effects, no matter how small, to modify the system response by preventing singularities.

Numerical solutions of the complete set of equations (1)–(5) were obtained using finite difference techniques. A Crank–Nicholson scheme second order accurate in time and space was used. The grid was staggered in time with the streamfunction being calculated at full time steps and the temperature at the intermediate half time steps. The grid overlapped the spatial boundaries by one grid interval. In order to achieve adequate resolution and verify the numerical properties of the scheme, different grid resolutions up to 320 intervals (323 points) were used. The response was investigated for Ra in the vicinity of the first Rayleigh–Bénard eigenvalue at 237.7, i.e., in the range $250<\mathrm{Ra}<500$. The qualitative nature of the solutions found in this regime of Ra is expected to remain unchanged for $\mathrm{Ra}<\mathrm{Ra}_{c2}\approx 2496.5$, the second Rayleigh–Bénard eigenvalue. The modulation frequency and Prandtl were varied in the range $0.01<\Omega<1$ and $0.1<\mathrm{Pr}<100$. Depending on the parameters, the number of time steps in a cycle of modulation ranged from 10^3 to 5×10^6. Evolution to the desired periodic solution was tested by examining the fluid velocity and temperature at the center of the slot as functions of time. Computations were carried out till converged periodic solutions were obtained.

The evolution of the system response was studied by following the velocity and temperature values at a fixed depth over a complete cycle. Values were recorded at various depths and for different parameter values. The behavior was found to be qualitatively similar for all variables. Also, the temperature waveforms were found to be similar to the velocity waveforms. Here we present the surface velocity as a measure of the system response.

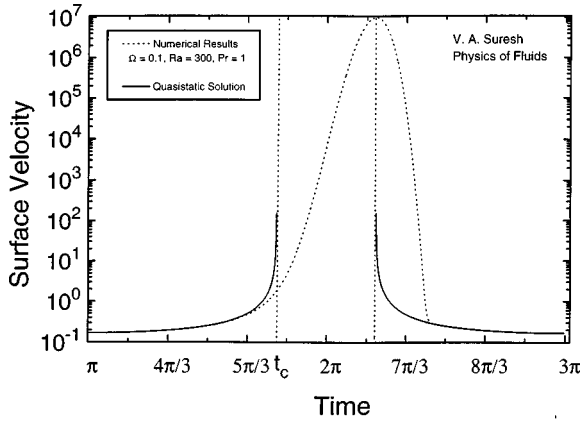

FIG. 2. Waveform of the response over one cycle showing the response at finite frequency contrasted with the divergence of the quasistatic solution.

Figure 2 shows a waveform of the surface velocity plotted for particular parameter values (Ra=300, Ω=0.1, Pr=1) across one time period. Figure 3 shows the same quantity as a function of $\mathrm{Ra}\cos(t)$. A time-periodic solution thus becomes a loop when plotted in this fashion. The quasistatic solution[7] is shown as a solid curve for comparison and it becomes infinite at the time, t_c, at which $\mathrm{Ra}\cos(t)=\mathrm{Ra}_c$. In the stable part of the cycle $[\cos(t)<0]$ and over part of the unstable part, the numerical solution closely matches the quasistatic solution. In the vicinity of the eigenvalue inertia slows the growth of the numerical solution, which is still small when the eigenvalue is reached. In the supercritical region beyond the eigenvalue, the numerical solution grows rapidly and reaches a very large maximum, but remains bounded. The extremely large velocity and temperature gradients caused by the resonant response makes the flow susceptible to secondary instabilities associated with finite wave number modes. These nonlinear effects could prevent the

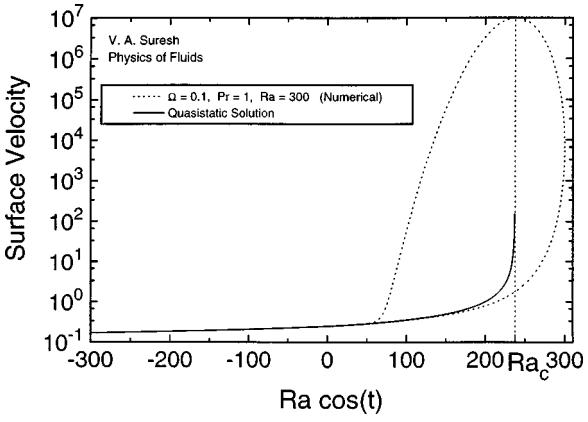

FIG. 3. Response over one cycle plotted as a function of $\mathrm{Ra}\cos(t)$. The waveform of Fig. 2 becomes a loop as shown.

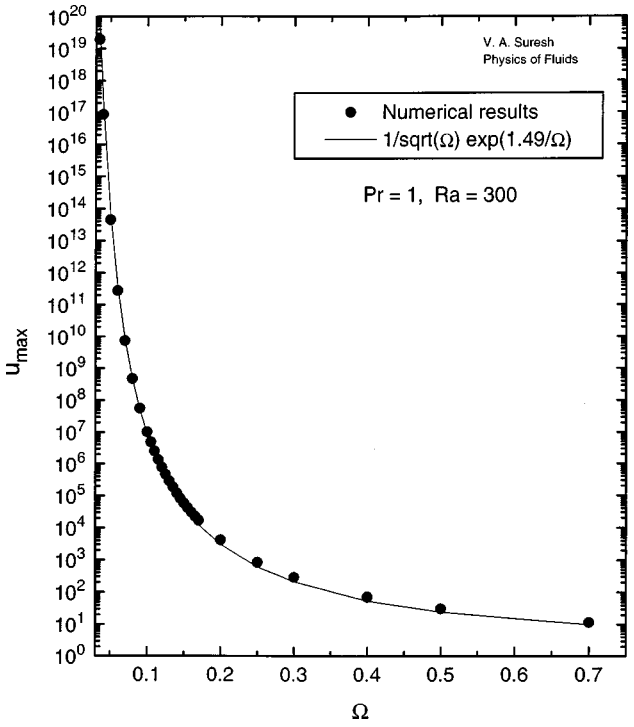

FIG. 4. Maximum response of the surface velocity against dimensionless frequency.

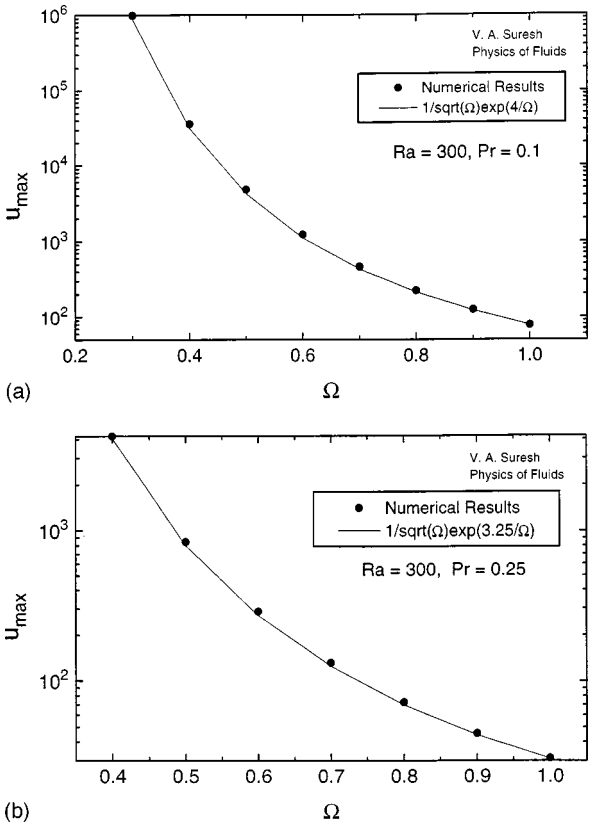

FIG. 5. Maximum response as a function of frequency for small Pr. (a) Pr=0.1 and (b) Pr=0.25.

response from reaching the magnitudes found here. However, we focus on developing a description of the long-wave response to the modulation and do not consider the effect of nonlinearities. Further, from Figs. 2 and 3 it is clear that inertia leads to a delay in the system response as it sweeps past the eigenvalue and the maximum occurs in the vicinity of the eigenvalue during the ''down swing'' as $\mathrm{Ra}\cos(t)$ decreases from its maximum value. The numerical solution rejoins the quasistatic solution as the system moves away from the eigenvalue. Thus it is clear that inertial effects are important only in a small region or inertial time boundary layer in the vicinity of the eigenvalue. This region is characterized by the rapid growth to a large response followed by a rapid decay.

E. Frequency scaling and parametric dependence of the resonant amplitude

The features described above are observed throughout the parameter space. Thus finite frequency modulation qualitatively changes the nature of the system response when compared to the quasistatic case by introducing features such as a finite response as the system becomes supercritical, a delay in the system response, and large, but bounded, resonant amplitudes. So, it is important to determine how these new features depend on parameters such as the modulation frequency and the Prandtl number.

In order to determine the frequency dependence of the resonant response, the system response was determined for various frequencies for fixed Ra and Pr. Figure 4 shows a plot of the maximum resonant amplitude of the surface velocity as a function of the modulation frequency for Ra=300 and Pr=1. Identical results were obtained for resonant temperature and resonant velocity amplitudes measured at other depths. The points represent numerical results while the dotted line shows a best fit given by

$$u_{\max} \sim \frac{1}{\sqrt{\Omega}} \exp\left(\frac{f(\mathrm{Ra},\mathrm{Pr})}{\Omega}\right) \tag{23}$$

with $f(\mathrm{Ra},\mathrm{Pr})=1.495$ for the choice of parameters here. The functional form of the fit is justified in the asymptotic analysis in the next section. The resonant amplitude is seen to increase exponentially with the reciprocal of the modulation frequency. This result can be attributed to the stabilizing effects of inertia. As we discuss in later sections, increased inertia limits the ultimate amplitude to which an unstable mode can grow. What cannot be anticipated until further analysis is done is the exponential dependence demonstrated in the figure.

In order to determine the Prandtl number dependence of the solutions, plots such as Fig. 4 were generated for various Pr, keeping Ra fixed. Figures 5(a) and 5(b) are plotted for small Pr=0.1 and 0.25, respectively while Figs. 6(a) and 6(b) are for large Pr=10 and 50. A best fit to the functional form, (23), was obtained for each Pr and Figs. 7(a) and 7(b) show the variation of $f(\mathrm{Ra},\mathrm{Pr})$ with Pr for small and large Pr, respectively.

Figure 7(a) suggests that as $\mathrm{Pr}\to 0$, $f(\mathrm{Ra},\mathrm{Pr})$ approaches a constant and becomes independent of Pr. So the resonant response depends only on the modulation frequency at fixed Ra as indicated by (23). Physically this result can be ex-

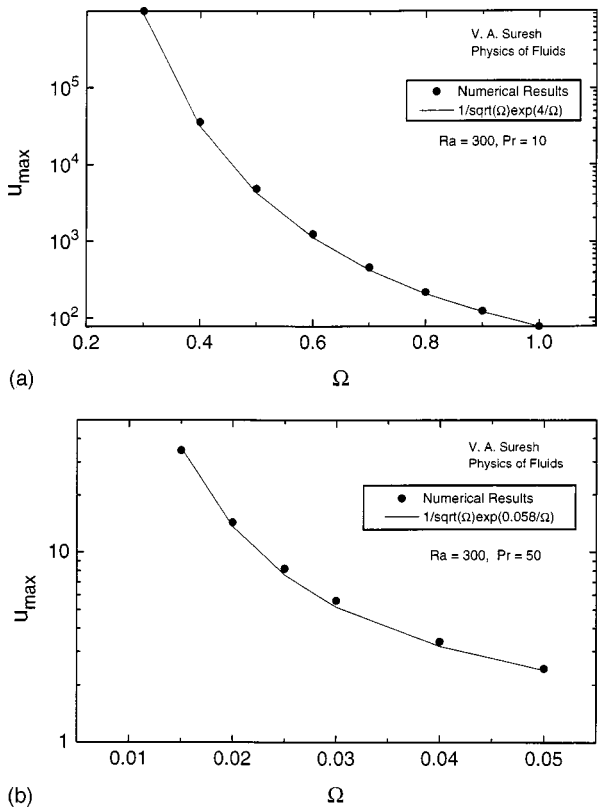

FIG. 6. Maximum response as a function of frequency for large Pr. (a) Pr=10 and (b) Pr=50.

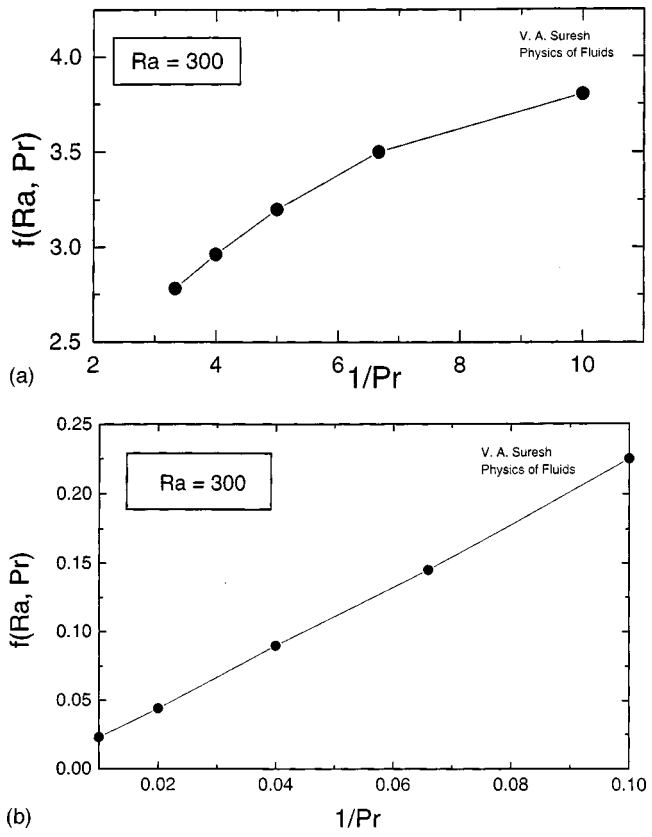

FIG. 7. The function $f(Ra,\mathrm{Pr})$ in the scaling law, Eq. (23) for fixed Ra. (a) Low Pr. (b) High Pr.

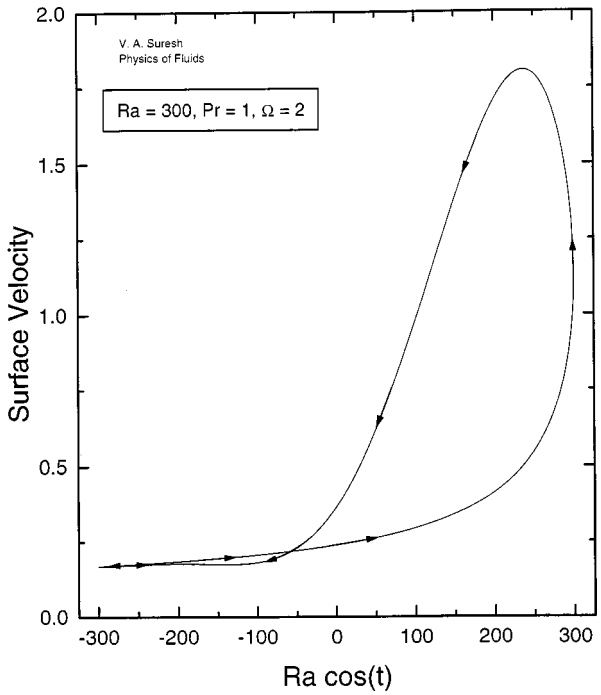

FIG. 8. Response curves showing relaxation oscillations for the indicated parameters.

plained by considering the dominant inertial effects. At small Prandtl numbers, the fluid inertia, measured by Ω, is much larger than the thermal inertia, measured by $\mathrm{Pr}\Omega$ and therefore controls the magnitude of the resonant response, which is independent of Pr.

Figure 7(b) shows that at large Pr, $f(\mathrm{Ra},\mathrm{Pr})\sim 1/\mathrm{Pr}$. So the resonant response scales as $\exp(1/Pr\Omega)$ at fixed Ra. The large Pr limit corresponds to thermal inertia $\mathrm{Pr}\Omega$ dominating fluid inertia, which then limits the magnitude of the response.

F. Relaxation oscillations

Relaxation oscillations are observed in the system response for fairly large Ω and $\mathrm{Pr}\sim O(1)$ as shown in Fig. 8, in which the surface velocity is plotted as a function of the instantaneous Rayleigh number. The arrows indicate the progression of time which is a parameter in the plot. This figure indicates that as the system returns to the stable part of the cycle, the surface velocity exhibits damped oscillations about its quasistatic value. The oscillations are observed as the large resonant response dies down, but are not present as the system moves from the stable part of the cycle to the unstable part. The fact that they are observed only when the fluid and thermal inertia are comparable suggests that the mechanism responsible for the oscillations involves a coupling of the fluid and thermal fields. This reasoning is borne out by the analysis in Sec. IV.

Oscillations were observed at all values of Ra considered, but the threshold values of Ω and Pr at which oscillations were first observed and the amplitude of the oscillations depended on Ra. As Ra was increased at constant Ω and Pr, higher amplitudes were observed, indicating that the amplitude of the oscillations depends on the time spent by the system in the supercritical regime. However, the qualitative

features of the oscillations are expected to remain unchanged between the first and second Rayleigh–Bénard eigenvalues

At a given Ra and Pr, oscillations were found to be absent below a threshold frequency, in keeping with the proposition that coupling of the fluid and thermal fields is responsible for them. Oscillations were also not observed at very high frequencies at which the resonant response was completely damped by inertia. For intermediate frequencies, oscillations of varying amplitudes were present which increased as the frequency was decreased. However, the amplitude of the oscillations relative to the resonant amplitude of the response increased with frequency.

In summary, the numerical analysis establishes that inertial effects resolve the singularities found in the quasistatic solution. The system response in the stable part of the cycle is found not to vary significantly from the quasistatic solution. However, the growth of the response in the unstable part is moderated by inertia, leading to a finite $O(\Omega^{-1/2}\exp(1/\Omega))$ response at the Rayleigh–Bénard eigenvalue. Inertia is also found to cause an $O(1)$ delay in the onset of the resonant response even for small Ω. The amplitude of the resonance is found to be depend on the finite frequency response at the eigenvalue as well as the time spent by the system in the supercritical part of the cycle. Relaxation oscillations are observed in a certain parameter range when the fluid and thermal inertias are comparable.

IV. ANALYTICAL RESULTS

A. Galerkin expansion

The coupled partial differential equations (1) and (2) do not admit a straightforward analytical analysis. Therefore, it is useful to develop an approximate theoretical approach in order to gain insight into the behavior of the system. The numerical solutions suggest that the system response is governed by resonance with the unstable Rayleigh–Bénard modes, so it is reasonable to assume that the spatial structure of the solution resembles the eigenfunctions of the long wave Rayleigh–Bénard modes described in Sec. III C. Under this assumption, it is possible to use a Galerkin expansion to decouple the time and spatial dependence of the equations and derive a dynamical system for the response.

We restrict our attention to instantaneous Rayleigh numbers that do not greatly exceed the first Rayleigh–Bénard eigenvalue, $\mathrm{Ra}_c \approx 237.7$. So, we use a one term Galerkin approximation and seek solutions of the form

$$\psi(y,t) = A(t)\overline{\psi}(y) + \psi_{\mathrm{SD}}(y), \tag{24}$$

$$T(y,t) = B(t)\overline{T}(y) + T_{\mathrm{SD}}(y). \tag{25}$$

Here $\overline{\psi}(y)$ and $\overline{T}(y)$ are the spatial eigenfunctions given by (16) and (20). ψ_{SD} and T_{SD} are the Sen and Davis solutions described in Sec. III A and are used homogenize the thermocapillary boundary condition (4).

Following the usual Galerkin procedure detailed in Appendix A, the following equation governing the time evolution of the system is obtained:

$$\mathrm{Pr}\Omega^2 B_{tt} + a_1\Omega(1+a_2\mathrm{Pr})B_t + a_3\left(1-\frac{\mathrm{Ra}\cos(t)}{\mathrm{Ra}_c}\right)B = a_4\mathrm{Ra}\cos(t), \tag{26}$$

where the $\{a_i\}$ are constants defined in Appendix A and are all positive. Here $A(t)$ has been eliminated from the dynamical system, but as a result of the general form of the energy equation, is always related to $B(t)$ as

$$A = B + \frac{\mathrm{Pr}}{a_1\Omega}B_t. \tag{27}$$

Equation (26) describes a damped and forced oscillator. The damping coefficient $a_1\Omega(1+a_2\mathrm{Pr})$ consists of two contributions: $a_1\Omega$ from the fluid inertia and $a_1a_2\mathrm{Pr}\Omega$ from the thermal inertia. This clearly indicates the role of inertia in limiting the system response. The forcing term $a_4\mathrm{Ra}\cos(t)$ results from the thermocapillary base flow or, equivalently, from the thermocapillary stress at the interface. The coefficient of the final term on the left, $a_3(1-\mathrm{Ra}\cos(t)/\mathrm{Ra}_c)$, is positive in the subcritical region, $\mathrm{Ra}\cos(t)<\mathrm{Ra}_c$ and acts as a restoring force. In the supercritical region it changes sign and acts as an energy input, leading to the large resonant response. Finally, the term $\mathrm{Pr}\Omega^2 B_{tt}$ represents the coupling of fluid and thermal inertia. We shall show later that this coupling is responsible for the relaxation oscillations observed in the numerical solutions.

B. Large and small Pr results

In general, it is complicated to obtain asymptotic solutions for the oscillator equation (26). Therefore, it is convenient to consider the limiting cases $\mathrm{Pr}\to 0$ and $\mathrm{Pr}\to\infty$, $\Omega\mathrm{Pr}\sim$ finite, in order to obtain simple analytical results for the frequency and parametric dependence. These limits correspond to dominant fluid and thermal inertia, respectively. This allows us to neglect the coupling of fluid and thermal inertia and thus (26) reduces to a first-order differential equation in both cases. Also, in the former case $a_1a_2\mathrm{Pr}\Omega B_t$ in (26) can be neglected compared to $a_1\Omega B_t$ while in the latter case $a_1\Omega B_t$ can be neglected compared to $a_1a_2\mathrm{Pr}\Omega B_t$. The structure of the differential equation is identical in both cases and can be represented by

$$B_t + \frac{\phi_t(t)}{\Omega}B = \frac{p}{\Omega}\mathrm{Ra}\cos(t), \tag{28}$$

where

$$\phi_t(t) = m\left(1-\frac{\mathrm{Ra}}{\mathrm{Ra}_c}\cos(t)\right), \tag{29}$$

and Ra_c is the critical Rayleigh number defined previously. The constants m and p depend on the particular limit being considered, and are defined as

$\underline{\mathrm{Pr}\to 0}$	$\underline{\mathrm{Pr}\to\infty}$
$A(t)=B(t)$	$A(t)=B+\dfrac{\mathrm{Pr}\Omega}{a_1}B_t$
$m=a_3/a_1$	$m=\dfrac{a_3}{\mathrm{Pr}a_2a_1}$
$p=a_4/a_1$	$p=\dfrac{a_4}{\mathrm{Pr}\,a_1a_2}$

Certain features of the numerical results are reproduced by (28). The quasistatic solution of (28) is given by

$$B_{qs}(t)=\frac{p\mathrm{Ra}\cos(t)}{\phi_t(t)}. \tag{30}$$

$B_{qs}(t)$ becomes infinite at a time $t=t_{c1}$ when $\mathrm{Ra}\cos(t)=\mathrm{Ra}_c$ and thus reproduces the breakdown of the quasistatic solution at the critical Rayleigh number.

The exact solution of (28) is given by

$$B(t)=\frac{p}{\Omega}\exp\left(-\frac{\phi(t)}{\Omega}\right)\int_0^t \mathrm{Ra}\cos(s)\exp\left(\frac{\phi(s)}{\Omega}\right)ds, \tag{31}$$

where

$$\phi(s)=m\left(s-\frac{\mathrm{Ra}}{\mathrm{Ra}_c}\sin(s)\right). \tag{32}$$

This solution is bounded at all times for nonzero Ω.

It is not possible to obtain an exact analytical expression for $B(t)$ from (31). However, asymptotic expressions for $B(t)$ can be developed for small Ω, as explained in Appendix B. It is possible to determine the scaling properties of the solution from these expressions.

The asymptotic analysis shows that in the subcritical part of the cycle $B(t)$, to leading order in Ω, takes the form

$$B(t)\sim\frac{p\,\mathrm{Ra}\cos(t)}{\phi_s(t)}=B_{qs}(t). \tag{33}$$

This indicates that the solution remains close to the quasistatic solution in the subcritical part of the cycle.

As the system approaches the critical point, this expression is replaced by

$$B(t)\sim p\,\mathrm{Ra}\cos(t)\sqrt{\frac{\pi}{-2\Omega\phi_{ss}(t)}}\times\exp\left(-\frac{\phi_s^2(t)}{2\Omega\phi_{ss}(t)}\right)\left[1-\mathrm{erf}\left(\frac{\phi_s(t)}{\sqrt{-2\Omega\phi_{ss}(t)}}\right)\right], \tag{34}$$

where erf is the error function. At the critical point $t=t_{c1}$ when the system crosses over into the supercritical regime, $\phi_s(t_{c1})=0$ and the solution reduces to

$$B(t_{c1})\sim p\mathrm{Ra}_c\sqrt{\frac{\pi}{-2\Omega\phi_{ss}(t_{c1})}}. \tag{35}$$

Thus the system response at the critical point is bounded and scales as $\Omega^{-1/2}$.

The asymptotic analysis also shows that in the supercritical region the solution grows exponentially and reaches a maximum given by

$$B(t)\sim p\,\mathrm{Ra}_c\sqrt{\frac{2\pi}{-\Omega\phi_{ss}(t_{c1})}}\exp\left(\frac{\phi(t_{c1})-\phi(t_{c2})}{\Omega}\right). \tag{36}$$

Here t_{c2} is the time at which the system returns to the subcritical regime, i.e when $\mathrm{Ra}\cos(t)=\mathrm{Ra}_c$. Thus the maximum occurs when the system crosses the Rayleigh–Bénard eigenvalue as indicated by the numerical results. This expression determines the frequency scaling of the resonant response which was used to determine a fit for the numerical results in Figs. 4–6. The Pr dependence can be retrieved by noting that m, and hence $\phi(t)$, is independent of Pr in the small Pr limit and scales as 1/Pr in the large Pr limit. Thus it is clear that the Galerkin approximation in the limit of extreme Prandtl numbers captures the qualitative features of the system response.

C. Pr∼O(1) results

The complete second-order oscillator equation (26) has to be considered when Pr∼O(1). However, it is sufficient to study the homogeneous form of the equation in order to determine the features of the solution:

$$\Omega^2B_{tt}+a_1\Omega\left(\frac{1}{\mathrm{Pr}}+a_2\right)B_t+\frac{a_3}{\mathrm{Pr}}\left(1-\frac{\mathrm{Ra}\cos(t)}{\mathrm{Ra}_c}\right)B=0. \tag{37}$$

The Wentzel–Kramers–Brillouin (WKB) method is used to analyze this equation as explained in Appendix C. This analysis shows that a suitable change of variable,

$$B(t)=\exp\left(\frac{-1}{2\Omega}\int_0^t a_1\left(\frac{1}{\mathrm{Pr}}+a_2\right)ds\right)Q(t), \tag{38}$$

transforms (37) into

$$\Omega^2Q_{tt}-\beta(t)Q=0, \tag{39}$$

where

$$\beta(t)=\frac{a_1^2(1/\mathrm{Pr}+a_2)^2}{4}+\frac{a_3}{\mathrm{Pr}}\left(\frac{\mathrm{Ra}\cos(t)}{\mathrm{Ra}_c}-1\right). \tag{40}$$

The WKB variable is then defined as

$$\sigma=\frac{1}{\Omega}\int\sqrt{\beta(t)}\,dt,\quad \beta(t)>0, \tag{41}$$

$$\sigma=\frac{i}{\Omega}\int\sqrt{-\beta(t)}\,dt,\quad \beta(t)<0, \tag{42}$$

and (39) has solutions of the form

$$Q(t)\sim b_1\exp(\sigma)+b_2\exp(-\sigma). \tag{43}$$

In the supercritical region, $\beta(t)>0$ and thus the system exhibits an exponentially large response. Also (43) retrieves the exponential scaling of the response with the inverse modulation frequency, which is in agreement with the numerical

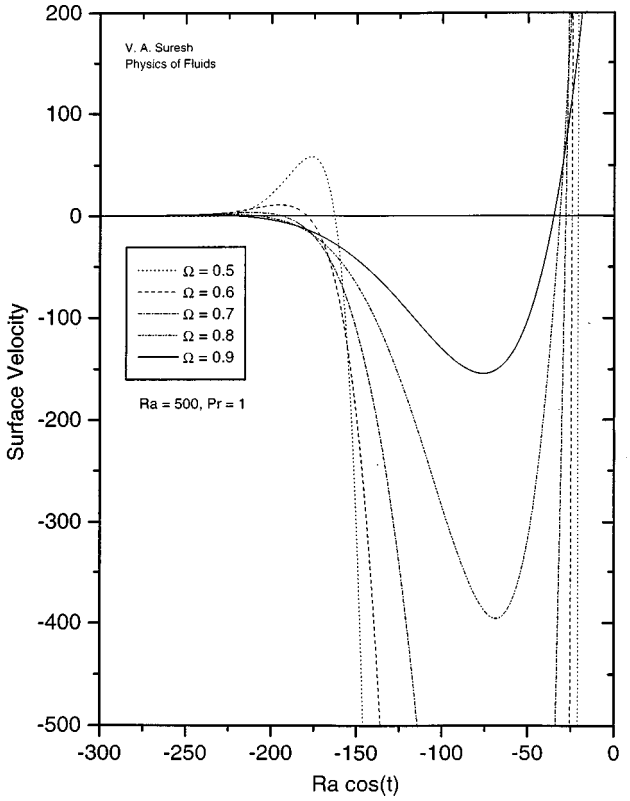

FIG. 9. Response curves showing the relaxation oscillations for a range of frequencies. Note that the range of $\mathrm{Ra}\cos(t)$ over which they occur is approximately constant.

results presented in Fig. 4. Thus the coupling of thermal and fluid inertia does not qualitatively change the nature of the frequency scaling.

This solution is also able to predict the occurrence of relaxation oscillations since (43) indicates that when $\beta(t) < 0$, the solution is oscillatory in nature. From the definition of β, it is found that the oscillations are predicted to occur in the stable part of the cycle when $\mathrm{Ra}\cos(t) < 0$, in accordance with the numerical results. Further, since $\beta(t)$ is independent of the modulation frequency, the range of $\mathrm{Ra}\cos(t)$ over which the relaxation oscillations are observed is also predicted to be independent of the modulation frequency. In Fig. 9, the relaxation oscillations obtained from numerical solution of the equations are plotted for different modulation frequencies at fixed Ra and Pr. It is found that the oscillations are indeed confined to a fairly constant range of $\mathrm{Ra}\cos(t)$, independent of Ω.

V. DISCUSSION AND SUMMARY

Our focus in this paper has been to study the effect of small but finite inertia on a modulated flow that crosses a bifurcation point in a periodic fashion. In the absence of inertia, the solution becomes infinite at the bifurcation point and the flow structure predicted for later parts of the cycle have no physical significance. Thus the study of finite inertia is required to remove both the unphysical singularity and to allow prediction of the flow structure and response for supercritical conditions. Numerical methods were used to obtain solutions of the complete set of governing equations and to determine the parametric dependence of the response. While the full solutions give ''exact'' numerical solutions, we found it helpful to develop a dynamical system for the response using truncated Galerkin expansions. The analytical solution for the dynamical system allows an asymptotic analysis which gives insight into the scalings and the physics which are also exhibited by the full numerical solutions.

As the system approaches the critical point, the flow in the slot is accelerated by the unstable stratification and, being a parallel flow, there are no nonlinearities to limit the response. However, finite inertia—either fluid or thermal inertia—retards this acceleration and the amplitude at criticality, while large, is bounded and scales as $O(\Omega^{-1/2})$. This finite response provides a starting point for the exponential growth of the solution in the supercritical region, as the flow now grows to large amplitude due to the fact that some of the eigenvalues of the system (either the dynamical system or the partial differential equations) are positive. This corresponds to an acceleration of the flow in the same sense as the underlying thermocapillary return flow, which serves to break the symmetry of the stability problem and also provide the ''forcing perturbation'' for the exponential growth. These inertial effects lead to an $O(1)$ delay in the system response for very small frequencies, i.e., the rapid growth is not coincident with the crossing of the bifurcation point, but takes some time due to the need to accelerate flow and temperature fields that have finite inertia. Exponential growth then occurs, as expected, until the modulation returns the Rayleigh number to a value below the critical, at which time the flows driven by disturbances start to decay.

Analytical results suggest a scaling for the maximum amplitude reached by the flow to be $\Omega^{-1/2}\exp(f/\Omega)$. The resonant response, measured by f, was found to be controlled by the dominant inertial effect. Therefore, in the fluid inertia controlled regime ($\mathrm{Pr}\to 0$), the response was found to be independent of Pr and to scale exponentially with the reciprocal of the modulation frequency Ω. Similarly in the thermal inertia dominant regime ($\mathrm{Pr}\to\infty$), there was an exponential dependence on $1/\mathrm{Pr}\Omega$.

Interestingly, coupling of the fluid and thermal fields was found to cause relaxation oscillations in the parameter ranges $\mathrm{Pr}\sim O(1)$ for fairly large Ω. That such oscillations should occur is made clear by examining the Galerkin approximations, in which the flow is either in phase or in antiphase with the temperature in the extremes of either high or low Pr [refer to the equations relating $A(t)$ and $B(t)$ following Eq. (26)]. Thus, in the process of the decay of perturbations back from the large resonant response to the thermocapillary return flow, the velocity and temperature components are of varying phase relationship to one another and oscillations ensue. If on the other hand, Pr takes either extreme, the phase is fixed and the decay is monotonic, being governed by either the fluid or thermal inertia. The threshold frequency for the onset of oscillations was found to increase as Ra was decreased at constant Pr.

Of course the flows computed here by either numerical or asymptotic methods are not expected to be stable, as they

represent very large velocities (and associated shear rates) and temperature gradients which would undoubtedly become unstable to shear and buoyancy instability modes characterized by finite wave numbers. While these are not considered in the present paper, the solutions found here, together with the development of a method of extending solutions past the bifurcation point, are an important first step in analyzing these secondary instabilities.

ACKNOWLEDGMENTS

Primary support for this work was through a grant from the Microgravity Science Division of NASA (Grant No. NAG3-1943). VAS gratefully acknowledges support from the Stanford Graduate Fellowship Program. CIC acknowledges support from the ACS-PRF through Grant No. PRF-28774-AC9.

APPENDIX A: GALERKIN APPROXIMATION

Approximate solutions of the form

$$\psi(y,t)=A(t)\overline{\psi}(y)+\psi_{\mathrm{SD}}(y), \tag{A1}$$

$$T(y,t)=B(t)\overline{T}(y)+T_{\mathrm{SD}}(y), \tag{A2}$$

where $\overline{\psi}(y)$ and $\overline{T}(y)$ are the Rayleigh–Bénard eigenfunctions discussed in Sec. III C and $\psi_{\mathrm{SD}}(y)$ and $T_{\mathrm{SD}}(y)$ are the thermocapillary return flow solutions, are assumed for the governing equations (1) and (2). Upon using these in the governing equations we obtain the following equations for the time evolution of the coefficients $A(t)$ and $B(t)$:

$$\Omega A_t\overline{\psi}_{yy}=A\overline{\psi}_{yyyy}+\mathrm{Ra}\cos(t)(B\overline{T}_y-\psi_{\mathrm{SD}}), \tag{A3}$$

$$\Omega\,\mathrm{Pr}B_t\overline{T}=A\overline{\psi}_y+B\overline{T}_{yy}. \tag{A4}$$

Following the usual Galerkin method, the inner product is defined as

$$\langle a,b\rangle=\int_0^1 ab^*\,dy, \tag{A5}$$

where the asterisk denotes the complex conjugate. Residuals are constructed by taking the inner product of (A3) with $\overline{\psi}$ and (A4) with $\overline{T}$. Upon setting the residuals equal to zero, the following pair of coupled, nonhomogeneous ordinary differential equations are obtained for A and B

$$\overline{c}_1\Omega A_t=-\overline{c}_2A+\overline{c}_2\mathrm{Ra}\cos(t)B-\overline{c}_3\mathrm{Ra}\cos(t),$$

$$\overline{c}_4\mathrm{Pr}\Omega B_t=\overline{c}_5A-\overline{c}_5B,$$

where

$$\overline{c}_1=\chi_+^2(\langle J_1,J_1\rangle\sin^2(\chi_+)-\langle H_1,H_1\rangle\sinh^2(\chi_+)),$$

$$\overline{c}_2=\chi_+^4(\langle H_1,H_1\rangle\sinh^2(\chi_+)+\langle J_1,J_1\rangle\sin^2(\chi_+)),$$

$$\overline{c}_3=\langle J_1,\psi_{\mathrm{SD}}\rangle\sin(\chi_+)-\langle H_1,\psi_{\mathrm{SD}}\rangle\sinh(\chi_+),$$

$$\overline{c}_4=\langle H_2,H_2\rangle\sinh^2(\chi_+)-2\langle H_2,J_2\rangle\times\sinh(\chi_+)\sin(\chi_+)+\langle J_2,J_2\rangle\sin^2(\chi_+),$$

$$\overline{c}_5=\chi_+^2(\langle J_2,J_2\rangle\sin^2(\chi_+)-\langle H_2,H_2\rangle\sinh^2(\chi_+)),$$

with H_i and J_i defined by Eqs. (17), (18), (21), and (22). Defining

$$c_2=\frac{\overline{c}_2}{\overline{c}_1},\quad c_3=\frac{\overline{c}_3}{\overline{c}_1},\quad c_5=\frac{\overline{c}_5}{\overline{c}_4}, \tag{A6}$$

the time evolution equations can be written as

$$\Omega A_t=-c_2A+c_2\mathrm{Ra}\cos(t)B-c_3\mathrm{Ra}\cos(t), \tag{A7}$$

$$\mathrm{Pr}\Omega B_t=c_5A-c_5B. \tag{A8}$$

The unknowns $A(t)$ and $B(t)$ are then determined by these equations and the requirement of periodic solutions.

Since (A8) is algebraic in A, A can be eliminated to obtain a single second-order equation in B, i.e.,

$$\mathrm{Pr}\Omega^2B_{tt}+a_1\Omega(1+a_2\mathrm{Pr})B_t+a_3\left(1-\frac{\mathrm{Ra}\cos(t)}{\mathrm{Ra}_c}\right)B=a_4\mathrm{Ra}\cos(t), \tag{A9}$$

where

$$a_1=c_5,$$

$$a_2=c_2/c_5,$$

$$a_3=c_5c_2,$$

$$a_4=c_5c_3.$$

APPENDIX B: ASYMPTOTIC EVALUATION OF $B(t)$

In this section we present an asymptotic analysis of the equation

$$B(t)=\frac{p}{\Omega}\exp\left(-\frac{\phi(t)}{\Omega}\right)\int_{t_0}^{t}\mathrm{Ra}\cos(s)\exp\left(\frac{\phi(s)}{\Omega}\right)ds, \tag{B1}$$

with

$$\phi(s)=m\left(s-\frac{\mathrm{Ra}}{\mathrm{Ra}_c}\cos(s)\right). \tag{B2}$$

We use Laplace's method[11] which is commonly used to determine the asymptotics of integrals of the form

$$I(\epsilon)=\int_a^b f(s)\exp\left(\frac{\theta(s)}{\epsilon}\right)ds,\quad \epsilon\to 0, \tag{B3}$$

where $f(s)$ and $\theta(s)$ are real and continuous functions. The method is based upon the idea that if $\theta(s)$ has a maximum in the interval $a\leqslant s\leqslant b$ at $s=c$, the leading order contribution to $I(\epsilon)$ is from a small neighborhood in the vicinity of c. Thus it is possible to approximate the integral by

$$I(\epsilon)\approx I(\epsilon,\delta)=\int_{N(\delta)}f(s)\exp\left(\frac{\theta(s)}{\epsilon}\right)ds, \tag{B4}$$

where $N(\delta)$ is a δ-neighborhood of c. The choice of δ is arbitrary {such that $N(\delta)$ lies in the interval $[a,b]$} and the final answer must not depend on the particular choice of δ.

Thus it is to necessary determine the maximum of $\phi(s)$ in the interval $[t_0,t]$. The effect of linear drift term, s, $\phi(s)$

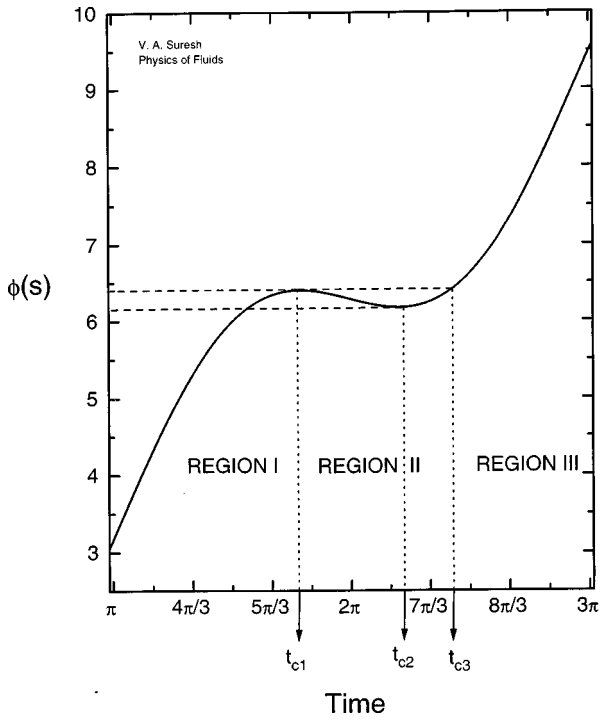

FIG. 10. Schematic showing the dependence of the integrating factor in the Galerkin equations as a function of time, with the definitions of the regions and times.

cancels out between the two exponentials in (B1) and therefore $B(t)$ has periodic solutions. Thus it is sufficient to evaluate the asymptotes of $B(t)$ in the course of a single time period. The variation of $\phi(s)$ in the time period $[\pi,3\pi]$ is sketched in Fig. 10. Depending on the value of t, three regions can be identified in Fig. 10. If t lies in regions I or III the maximum occurs at the end point of the interval $s=t$. In Fig. 10, region I corresponds to the interval $[\pi,t_{c1}]$, where t_{c1} is a local maximum of $\phi(s)$ and is defined by $\phi_s(t_{c1})=1-\mathrm{Ra}\cos(t_{c1})/\mathrm{Ra}_c=0$. So t_{c1} corresponds to the Rayleigh–Bénard eigenvalue and region I is the subcritical part of the cycle. Region III comprises of the interval $[t_{c3},3\pi]$ where t_{c3} is defined by the condition $\phi(t_{c1})=\phi(t_{c3})$ as shown in Fig. 10. Region II then is the interval $[t_{c1},t_{c3}]$ and contains within it the supercritical part of the cycle, $[t_{c1},t_{c2}]$. If t lies in region II, the maximum occurs at $s=t_{c1}$. In each of these regions, Laplace's method provides asymptotic evaluations of the integral in (B1).

1. Region I

Since the leading order contribution is from the vicinity of $s=t$, $\phi(s)$ can be approximated by a Taylor expansion about t:

$$\phi(s)\approx\phi(t)+\phi_s(t)(s-t), \tag{B5}$$

and the integral takes the form

$$B(t)\sim\frac{p}{\Omega}\mathrm{Ra}\cos(t)\int_{t-\delta}^{t}\exp\left(\frac{\phi_s(t)(s-t)}{\Omega}\right)ds. \tag{B6}$$

Here $\delta>0$ is an arbitrary number such that $t-\delta\geqslant t_0$. This integral can be evaluated to give

$$B(t)\sim\frac{p}{\Omega}\mathrm{Ra}\cos(t)\frac{1}{\phi_s(t)}\left(1-\exp\left(\frac{-\delta}{\Omega}\right)\right)$$

$$\sim\frac{p}{\Omega}\mathrm{Ra}\cos(t)\frac{1}{\phi_s(t)}. \tag{B7}$$

The last approximation is valid since $\exp(-\delta/\Omega)$ is exponentially small compared to 1. Thus the final asymptotic result is independent of the choice of δ.

This expression is valid away from t_{c1}. The one-term Taylor expansion is not accurate in the vicinity of t_{c1} since $\phi_s(t)$ is close to zero. In this case a two-term expansion is used:

$$\phi(s)\approx\phi(t)+\phi_s(t)(s-t)+\frac{\phi_{ss}(t)}{2}(s-t)^2. \tag{B8}$$

Now the integral takes the form

$$B(t)\sim\frac{p}{\Omega}\mathrm{Ra}\cos(t)\exp\left(-\frac{\phi_s^2(t)}{2\Omega\phi_{ss}}(t)\right)$$

$$\times\int_{t-\delta}^{t}\exp\left(\frac{\phi_{ss}(t)}{2\Omega}\left(s-\left(t-\frac{\phi_s(t)}{\phi_{ss}(t)}\right)\right)^2\right)ds. \tag{B9}$$

Since $\phi_{ss}(t)<0$ near the local maximum of $\phi(s)$ at $s=t_{c1}$, the integrand is the exponential of a negative quantity. This enables us to replace the lower limit of integration by $-\infty$ since the contribution to the final result from the interval $[-\infty,t-\delta]$ is negligible. After some manipulation, the above equation can be written in terms of the error function as

$$B(t)\sim p\mathrm{Ra}\cos(t)\sqrt{\frac{\pi}{-2\Omega\phi_{ss}(t)}}$$

$$\times\exp\left(-\frac{\phi_s^2(t)}{2\Omega\phi_{ss}(t)}\right)\left[1-\mathrm{erf}\left(\frac{\phi_s(t)}{\sqrt{-2\Omega\phi_{ss}(t)}}\right)\right], \tag{B10}$$

where

$$\mathrm{erf}(s)=\frac{2}{\sqrt{\pi}}\int_0^s\exp(-u^2)\,du \tag{B11}$$

is the error function.

When t is relatively far from t_{c1}, the argument of the error function is large. For large s, it can be shown by integration by parts that

$$\mathrm{erf}(s)\sim1-\frac{1}{s}\exp(-s^2). \tag{B12}$$

This shows that away from t_{c1}, (B10) reduces to (B7).

2. Region II

In this region the leading order contribution is from the vicinity of $s=t_{c1}$. A Taylor expansion about this point gives

$$\phi(s)\approx\phi(t_{c1})+\frac{\phi_{ss}(t_{c1})}{2}(s-t_{c1})^2, \tag{B13}$$

since $\phi_s(t_{c1})=0$. Following the previous development, it is then straightforward to show that

$$B(t)\sim p\mathrm{Ra}_c\sqrt{\frac{\pi}{-2\Omega\phi_{ss}(t_{c1})}}\exp\left((\phi(t_{c1})-\phi(t))/\Omega\right)\times\left[1+\mathrm{erf}\left(\sqrt{\frac{-\phi_{ss}(t_{c1})}{2\Omega}}(t-t_{c1})\right)\right]. \tag{B14}$$

Thus the solution is exponentially large in region II. As t moves away from t_{c1} the error function approaches 1 and $B(t)$ attains its maximum when $\phi(t)$ passes through its local minimum at $t=t_{c2}$. This point is defined by $\phi_s(t_{c2})=0$ and thus corresponds to the Rayleigh–Bénard eigenvalue. The maximum is thus given by

$$B(t)\sim p\mathrm{Ra}\cos(t_{c1})\sqrt{\frac{2\pi}{-\Omega\phi_{ss}(t_{c1})}}\times\exp\left((\phi(t_{c1})-\phi(t_{c2}))/\Omega\right).$$

3. Region III

As the upper limit of the interval, t, increases beyond t_{c2}, $\phi(t)$ increases as seen in Fig. 10 and $B(t)$ in (B14) starts decreasing. Eventually as t crosses t_{c3} the leading order contribution comes from the vicinity of t. In this case the analysis of region I is applicable and the solution is given by (B7).

Equations (B7), (B10), and (B14) thus provide the complete asymptotic solutions for $B(t)$. These expressions are valid over any time period $[(2n+1)\pi,(2n+3)\pi]$, $n=0,1,2\ldots.$

APPENDIX C: WKB ANALYSIS

The WKB procedure[11] is used to analyze the homogeneous form of (26):

$$\Omega^2B_{tt}+a_1\Omega\left(\frac{1}{\mathrm{Pr}}+a_2\right)B_t+\frac{a_3}{\mathrm{Pr}}\left(1-\frac{\mathrm{Ra}\cos(t)}{\mathrm{Ra}_c}\right)B=0. \tag{C1}$$

A Liouville transformation

$$B(t)=\exp\left(\frac{-1}{2\Omega}\int_0^t a_1\left(\frac{1}{\mathrm{Pr}}+a_2\right)ds\right)Q(t) \tag{C2}$$

transforms (C1) into a form suitable for WKB analysis:

$$\Omega^2Q_{tt}-\beta(t)Q=0, \tag{C3}$$

where

$$\beta(t)=\frac{a_1^2\left(1/\mathrm{Pr}+a_2\right)^2}{4}+\frac{a_3}{\mathrm{Pr}}\left(\frac{\mathrm{Ra}\cos\left(t\right)}{\mathrm{Ra}_c}-1\right). \tag{C4}$$

Since the $\{a_i\}$ are all positive, $\beta(t)$ has two zeroes in the course of a time period at $t=t_0$ and $t=2\pi-t_0$. Away from the zeroes the usual WKB analysis is followed by defining a new variable

$$\sigma=\frac{1}{\Omega}\int\sqrt{\beta(t)}\,dt,\quad \beta(t)>0, \tag{C5}$$

$$\sigma=\frac{i}{\Omega}\int\sqrt{-\beta(t)}\,dt,\quad \beta(t)<0. \tag{C6}$$

These give the solutions to leading order in Ω as

$$Q(t)=\beta(t)^{-1/4}(l_1\cosh(\sigma)+l_2\sinh(-\sigma)),\quad \beta(t)>0, \tag{C7}$$

$$Q(t)=(-\beta(t))^{-1/4}(m_1\cos(\sigma)+m_2\sin(\sigma)),\quad \beta(t)<0. \tag{C8}$$

These solutions are not valid at the turning point. In the vicinity of t_0, a new variable $\zeta=t-t_0$ is defined and $\beta(t)$ is approximated as $\beta(t)\sim f(\mathrm{Ra},\mathrm{Pr})\zeta+O(\zeta^2)$. Equation (C3) can then be written as

$$\Omega^2Q_{\zeta\zeta}=f(\mathrm{Ra},\mathrm{Pr})\zeta Q. \tag{C9}$$

Another change of variable $\xi=(f(\mathrm{Ra},\mathrm{Pr}))^{1/3}\Omega^{-2/3}\zeta$ reduces (C10) to the standard form

$$Q_{\xi\xi}=\xi Q, \tag{C10}$$

which admits the solution

$$Q(\xi)=p_1Ai(\xi)+p_2Bi(\xi), \tag{C11}$$

where $Ai(\xi)$ and $Bi(\xi)$ are the Airy functions.

Matching (C11) with (C7) in the limit $\xi\to\infty,\zeta\to t_0^-$ and with (C8) in the limit $\xi\to-\infty,\zeta\to t_0^+$ results in the following relations between the constants of integration:

$$l_2=2l_1,$$

$$m_1=m_2=2\sqrt{2}a_1,$$

$$p_1=p_2=\sqrt{2}\pi(f(\mathrm{Ra},\mathrm{Pr})\Omega)^{-1/6}.$$

This provides a complete solution of (37) to leading order in Ω.

[1] S. Chandrasekhar, *Hydrodynamic and Hydromagnetic Stability* (Dover, New York, 1981).
[2] G. K. Batchelor, ''Heat transfer by free convection across a closed cavity between vertical boundaries at different temperatures,'' Q. Appl. Math. **12**, 209 (1954).
[3] P. M. Gresho and R. L. Sani, ''The effects of gravity modulation on the stability of a heated fluid layer,'' J. Fluid Mech. **40**, 783 (1970).
[4] A. Farooq and G. M. Homsy, ''Streaming flows due to *g*-jitter-induced natural convection,'' J. Fluid Mech. **271**, 351 (1994).
[5] J. I. D. Alexander, ''Low gravity experiment sensitivity to residual acceleration: A review,'' Microgravity Sci. Technol. **III**(2), 52 (1990).
[6] A. Farooq and G. M. Homsy, ''Linear and non-linear dynamics of a differentially heated slot under gravity modulation,'' J. Fluid Mech. **313**, 1 (1996).
[7] P. Grassia and G. M. Homsy, ''Thermocapillary and buoyant flows with low-frequency jitter. I. Jitter confined to the phase,'' Phys. Fluids **10**, 1273 (1998).
[8] J. Hale and H. Kocak, *Dynamics and Bifurcations* (Springer-Verlag, Berlin, 1991).
[9] T. Erneux, E. L. Reiss, L. J. Holden, and M. Georgiou, ''Slow Passage Through Bifurcation and Limit Points. Asymptotic Theory and Applications,'' in *Dynamic Bifurcations*, edited by E. Benoit (Springer-Verlag, Berlin, 1991), pp. 14–29.
[10] A. K. Sen and S. H. Davis, ''Steady thermocapillary flows in two-dimensional slots,'' J. Fluid Mech. **121**, 163 (1982).
[11] C. M. Bender and S. A. Orszag, *Advanced Mathematical Methods for Scientists and Engineers* (McGraw–Hill, New York, 1978).